



A comprehensive study on meltpool depth in laser-based powder bed fusion of Inconel 718

Downloaded from: <https://research.chalmers.se>, 2026-04-06 02:14 UTC

Citation for the original published paper (version of record):

Khorasani, M., Ghasemi, A., Leary, M. et al (2022). A comprehensive study on meltpool depth in laser-based powder bed fusion of Inconel 718. *International Journal of Advanced Manufacturing Technology*, 120(3-4): 2345-2362. <http://dx.doi.org/10.1007/s00170-021-08618-7>

N.B. When citing this work, cite the original published paper.



A comprehensive study on meltpool depth in laser-based powder bed fusion of Inconel 718

Mahyar Khorasani^{1,2} · AmirHossein Ghasemi³ · Martin Leary¹ · Laura Cordova⁴ · Elmira Sharabian¹ · Ehsan Farabi⁵ · Ian Gibson^{2,6} · Milan Brandt¹ · Bernard Rolfe²

Received: 3 September 2021 / Accepted: 18 December 2021
© The Author(s) 2022

Abstract

One problematic task in the laser-based powder bed fusion (LB-PBF) process is the estimation of meltpool depth, which is a function of the process parameters and thermophysical properties of the materials. In this research, the effective factors that drive the meltpool depth such as optical penetration depth, angle of incidence, the ratio of laser power to scan speed, surface properties and plasma formation are discussed. The model is useful to estimate the meltpool depth for various manufacturing conditions. A proposed methodology is based on the simulation of a set of process parameters to obtain the variation of meltpool depth and temperature, followed by validation with reference to experimental test data. Numerical simulation of the LB-PBF process was performed using the computational scientific tool “Flow3D Version 11.2” to obtain the meltpool features. The simulation data was then developed into a predictive analytical model for meltpool depth and temperature based on the thermophysical powder properties and associated parameters. The novelty and contribution of this research are characterising the fundamental governing factors on meltpool depth and developing an analytical model based on process parameters and powder properties. The predictor model helps to accurately estimate the meltpool depth which is important and has to be sufficient to effectively fuse the powder to the build plate or the previously solidified layers ensuring proper bonding quality. Results showed that the developed analytical model has a high accuracy to predict the meltpool depth. The model is useful to rapidly estimate the optimal process window before setting up the manufacturing tasks and can therefore save on lead-time and cost. This methodology is generally applied to Inconel 718 processing and is generalisable for any powder of interest. The discussions identified how the effective physical factors govern the induced heat versus meltpool depth which can affect the bonding and the quality of LB-PBF components.

Keywords Additive manufacturing · Meltpool depth · Laser-based powder bed fusion · Laser irradiation · Wavelength

✉ Mahyar Khorasani
mahyar.khorasani@rmit.edu.au

✉ Martin Leary
martin.leary@rmit.edu.au

AmirHossein Ghasemi
amir_hosein_ghasemi2012@yahoo.com

Laura Cordova
laura.cordova@chalmers.se

Elmira Sharabian
s3913935@student.rmit.edu.au

Ehsan Farabi
ehsan.farabi@deakin.edu.au

Ian Gibson
i.gibson@utwente.nl

Milan Brandt
milan.brandt@rmit.edu.au

Bernard Rolfe
bernard.rolfe@deakin.edu.au

¹ School of Engineering, Royal Melbourne Institute of Technology, Melbourne, VIC, Australia

² School of Engineering, Deakin University, Geelong, VIC, Australia

³ Australian Institute of Science & Technology, Ashfield, NSW, Australia

⁴ Department of Industrial and Materials Science, Chalmers University of Technology, Gothenburg, Sweden

⁵ Insitute for Frontier Material, Deakin University, Geelong, VIC, Australia

⁶ Fraunhofer Project Centre for Complex System Engineering, Department of Design, Production, and Management, University of Twente, Enschede, The Netherlands

1 Introduction

Laser-based powder bed fusion (LB-PBF) is one of the classified additive manufacturing (AM) processes that produce metal components [1–3]. The induced heat source in LB-PBF produces heat penetration within the powder bed and solidified metal, where the meltpool depth is always smaller than the heat penetration depth due to conductive heat transfer [4, 5]. Different approaches have been developed for characterising the meltpool geometry based on process parameters in the LB-PBF of metals [6].

King et al. [7] characterised the meltpool track in three physical sections: a topological depression, a transition and a tail region and discussed different pore formation mechanisms in different regions of the meltpool. They discussed various fundamental physical phenomena in the meltpool such as depression formation, depression collapse and pore formation mechanisms, denudation, spatter formation and formation of lateral shallow pores. King et al. [8] also discussed the conditions in LB-PBF that lead to a transition from the conduction mode to the keyhole mode in the processing of stainless steel 316L. Observations were concluded by discussing the morphology of the meltpool track and more specifically meltpool depth. They introduced the threshold for transition from conduction mode to keyhole mode that is a function of process parameters, induced heat and enthalpy of fusion on the surface of the powder bed. Surface tension was introduced as one of the driving factors for meltpool formation and consolidation of melt-track in LB-PBF of stainless steel 316L. Surface tension was shown to be the critical factor that binds the meltpool and increases the contact area with the substrate. Therefore, it is a driving factor for smoothing the melt-track and improving heat transfer to the substrate, which consequently will affect meltpool depth [9]. Ciales et al. [10] studied the effect of process parameters on meltpool size and shape of Inconel 625 using in situ thermal camera video recording and spatter analysis. The study showed that meltpool geometry is constantly changing by moving the laser beam in the scan track. The in situ thermal video imaging showed approximately 20–35% of the total meltpool area spattered along a single track, leading to substantial loss of powder material and heat. Meltpool geometry and morphology variability of Inconel 718 produced by LB-PBF was studied by Scime and Beuth [11]. The authors investigated the single track of a powder-bed experiment to simulate an actual printing condition compared to a bare substrate. The cross-sectional morphology of the meltpools was affected by defects such as porosity, balling and keyholes. Compared to conduction mode, it is observed that the meltpool depth in keyhole mode is

more stable, notably when fewer defects appear in the meltpool. Scime and Beuth [12] developed an in situ system to detect the keyhole, porosity and balling by using a visible light high-speed camera. The authors stated that an in situ system that works based on unsupervised machine learning may indicate flaws such as those observed ex situ. It is found that the integration of the ex situ and in situ systems enables the use of supervised machine learning to better observe the meltpool features.

Hooper [13] measured the meltpool temperature by using coaxial imaging and a high-speed thermal camera. He mentioned that this system can have some limitations and errors but, the meltpool temperature can provide a robust benchmark to predict meltpool size and define acceptable process windows. Zhang et al. [14] evaluated the accuracy of different heat source models including cylindrical, semi-spherical, semi-ellipsoidal and conical distributions. They also investigated other heat source models such as radiation transfer, ray-tracing, linear decay and exponential decay methods to predict the meltpool dimension. They concluded that coupling a three-dimensional heat transfer model and the inconstant laser absorptivity model can significantly improve the result on meltpool morphology detection. Distinction of meltpool shape for different melting modes in a LB-PBF process is crucial in understanding the process better and to have defect-free components. Patel and Vlasea [15] developed a normalised processing diagram to visualise the three melting modes for an LB-PBF process. In this study, a third melting mode named “Transition Mode” was introduced, which is the region between conduction and keyhole mode. The distinction between these three melting modes is mainly defined with respect to the shape of the meltpool and the angle of evaporation (the angle between evaporation stream and normal line to the surface). Experimental validation for this normalised processing diagram was conducted for a few different metal materials commonly used in LB-PBF, and the meltpool morphology was considered as the distinguishing factor between the three melting modes. Results provided the possibility to predict the process parameters for different materials based on the normalised processing diagram. Keshavarzkermani et al. [16] studied the variation of laser power and scan speed on the meltpool geometry of Hastelloy produced by LB-PBF. The study showed that even with the same energy density, by changing the value of laser power and scan speed (in such a way to obtain the same aspect ratio), meltpool depth varies from 41.8 to 94 μm . This significant variation was also reported by Aversa et al. [17] in LB-PBF of AlSi10Mg, which is attributed to higher temperatures at the central meltpool zone and subsequently a higher plume and recoil pressure. Another factor that can

influence meltpool depth is the absorptivity of the laser, as reported by Ye et al. [18]. A coupled hydrodynamic finite element model and ray-tracing-based absorptivity model estimated absorption in different sets of process parameters. Experiments revealed that the meltpool depth is highly related to the ratio of normalised enthalpy to normalised diffusion length. Reijonen et al. [19] showed that the use of shielding gas improves the quality of the LB-PBF component as the obstruction of the laser beam by the process-induced vapour plume emissions reduces the laser penetration depth and subsequently shallowing the meltpool depth. The vapour plume is removed by the shielding gas flow and can significantly change the meltpool geometry. A practical solution to have a stable meltpool is using pulsed wave and continuous-wave lasers in a single printing process or using monitoring devices such as coaxial imaging and high-speed thermal cameras. Such controlling systems increase the price of the LB-PBF system as well as the ongoing maintenance costs [20].

It is practical to have a comprehensive model to predict the meltpool depth based on generalised properties that can be applied to different materials. Therefore, in this investigation, a simulation of LB-PBF for different process parameters has been carried out to find the meltpool temperature and depth for Inconel 718. Then, based on the thermophysical properties of the powder and induced energy density derived from the processing parameters, a physical model is developed to estimate the meltpool depth. The model aims to support process parameter selection in such a way that the laser penetration depth is enough to ensure an optimal bonding between the layers and therefore improve the quality of printed components. The results of the simulation and analytical model are compared with the experimental tests. Also, the governing phenomena which drive the meltpool depth versus induced energy are discussed to identify the leading mechanisms. In the next sections, simulation-related materials, results of temperature, meltpool depth and development of the predictor model are presented. Then, verification with experimental test cases is discussed, and the last section is dedicated to driving factors for meltpool depth such as optical penetration depth, angle of incidence, a ratio of laser power to scan speed, surface properties and plasma formation.

2 Simulation

Some of the studied simulations found in the literature [21, 22] are based on the solid substrate and neglect Marangoni convection. This means that the meltpool depth in the solid substrate and in the powder bed cannot be distinguished considering using these models. To provide

an accurate simulation, a scientific computational tool (Flow3D Version 11.2) has been used.¹ This computational software simulates a real powder-laser interaction using the governing mechanisms of LB-PBF and determines full multiphysics features such as fluid flow, the effect of Marangoni convection, heat transfer, solidification, powder particle distribution and powder packing density. The software also allows the selection of process parameters and preheating temperature. The simulation is based on the thermomechanical and thermophysical properties of the powder and works in both micro and mesoscale. It is known that metal evaporation has a significant effect on thermal history in LB-PBF and should not be overlooked [21, 23]. Thus, the evaporation and related effects are determined by Flow3D to improve the accuracy of the results in both conduction and keyhole modes.

2.1 Discrete element method

Due to multiple reflections of the laser beam amongst powder particles, the absorption ratio of the laser is different when the bed is covered by powder compared to a solid bed. To achieve realistic LB-PBF conditions, the powder bed was simulated by a computational software. The solver method is based on the discrete element method (DEM) that simulates the behaviour of discrete interacting bodies. The time step in the numerical solver is one of the significant factors that can drive the accuracy of the results. In this experiment the time-set size (Δt) was selected based on the minimum radius of powder particles, R_m (10 μm); scan speed, v ; density, ρ and elasticity, E , as shown in Eq. (1) [24]:

$$\Delta t = \frac{\pi R_{\min} \sqrt{\rho/E}}{0.163v + 0.877} \quad (1)$$

2.2 Heat modes in LB-PBF

Based on the amount of heat and absorptivity of the powder, conduction and keyhole modes are formed in the LB-PBF [8, 25, 26]. The commonly used conditions in an LB-PBF process result in material vaporisation irrespective of the melting modes (conduction or keyhole). These two modes are defined when heating up the feedstock in the laser processing of the metals. This depth of vaporisation is the driving factor for the threshold between the different melting modes [27, 28]. Fabbro and Chouf [29] have modelled the relationship between the extent of vaporisation and the incident beam spot diameter with the help of the front vaporisation angle.

¹ Flow3D commercial computational software Version 11.2.

Keyhole mode is commonly associated with high energy density where the laser has a large penetration depth into the powder. Additionally, if the beam is simulated by a Gaussian model, the evaporation starts from the centre region of the beam [30].

The total amount of laser energy in the LB-PBF process is calculated by Eq. (2). ED in Eq. (2) is laser energy density and other parameters are laser power (L_p), laser scanning speed (S_s), beam radius (B_r) and layer thickness (L_t). The fraction of absorbed energy by powder is determined by the absorption ratio (η) that is related to the nature of the material, thermophysical properties and temperature:

$$E_d = \frac{\eta L_p}{S_s B_r L_t} \tag{2}$$

The keyhole mode is mathematically represented by a body heat source, q_{body} , as a function of laser power, L_p ; heating depth, h and beam body radii, r_2 , that is distributed at both the surface and throughout the depth of the meltpool (Eq. 4) [31]. In contrast, if the energy of the heat source is relatively low, the conduction mode occurs and laser energy is primarily absorbed by powder at the upper surface of the powder bed, and minimal laser penetration occurs. The conduction mode is mathematically represented by a surface heat source, $q_{surface}$, that is distributed on the powder bed surface as a function of beam surface radius, r_1 (Eq. 3) [31]. Based on the magnitude of the induced surface energy on the powder bed, the computational software selects the surface heat source model for the conduction mode, or the body heat source model for the keyhole mode. In other words, if the energy density exceeds that required to induce melting of the bulk material, the body heat source is selected by the software:

$$q_{surface}(x, y) = \frac{3L_p e_1}{\pi r_1^2} e^{\left(\frac{-3(x^2+y^2)}{r_1^2}\right)} \tag{3}$$

$$q_{body}(x, y, z) = \frac{3L_p e_2}{\pi(1 - e^{-3})hr_2^2} e^{\left(\frac{-3(x^2+y^2)}{r_2^2}\right)} \tag{4}$$

In the current simulation, as a beam with a 50- μm diameter is used, r_1 is set at 50 μm , and “ r_2 ” is calculated by the software. The most important process parameters that drive the induced heat in LB-PBF are laser power, scan speed and beam diameter [32, 33]. The exact value of absorptivity is related to different parameters such as emissivity and the temperature of the system. Finding this relation is very complex, more so when printing is carried out on the powder bed. One common practice is finding the constant value for the specific temperature range. For Inconel 718 in the melting temperature, the constant value of absorptivity of 0.45 was selected for all test cases [34, 35]. Therefore, to investigate both keyhole and conduction modes, we used different process parameters and laser power/scan speed ratios.

2.3 Model geometry and boundary conditions

In total, 50,000 powder particles with normally distributed different particle sizes from 10 to 20 μm were selected to be matched with the verification experiment. Powders are compactly laid out with the recoater blade in such a way that the upper layers of the powders can freely move above the associated sublayers (Fig. 2). This helps to quantify the evolution of the powders under irradiation of various laser powers and simulates the physical interaction of the laser beam and the powder bed. In powder particle modeling, two interactions comprising particle–particle and particle–mesh walls are important. The powder particles are deposited on the build plate that acts as a substrate. Particles are layered on Z-direction, and the powder packing density is determined by the organisation of powder particles on the build platform. Powder packing density is adapted to the particle size and can be varied in the computational software. In LB-PBF, the powder packing density depends on different factors such as solid bed and recoater size, shape and speed. To obtain a suitable particle separation and packing density, a distance of 20 μm was maintained between the powder bed and recoater. The powder bed is deposited on a solid substrate that was designed in SolidWorks and converted to STL as shown in grey in Fig. 1.

To provide a compromise between solver efficiency and simulation resolution, a mesh size of 5 μm was

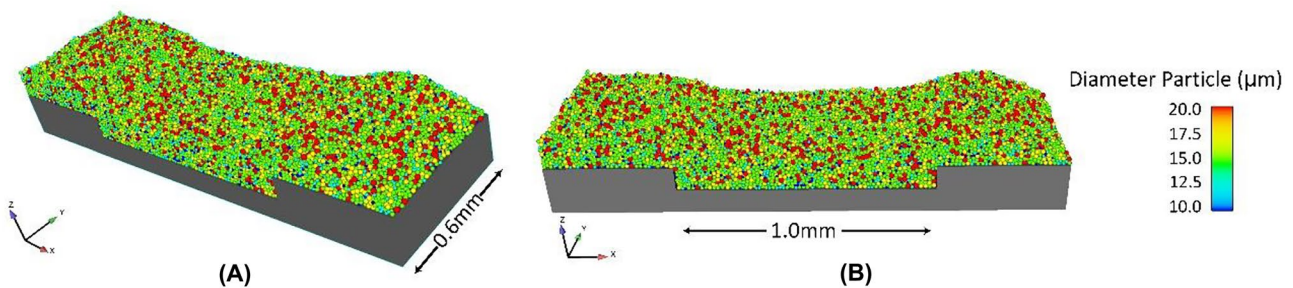


Fig. 1 Geometry of the powder bed and size in different views

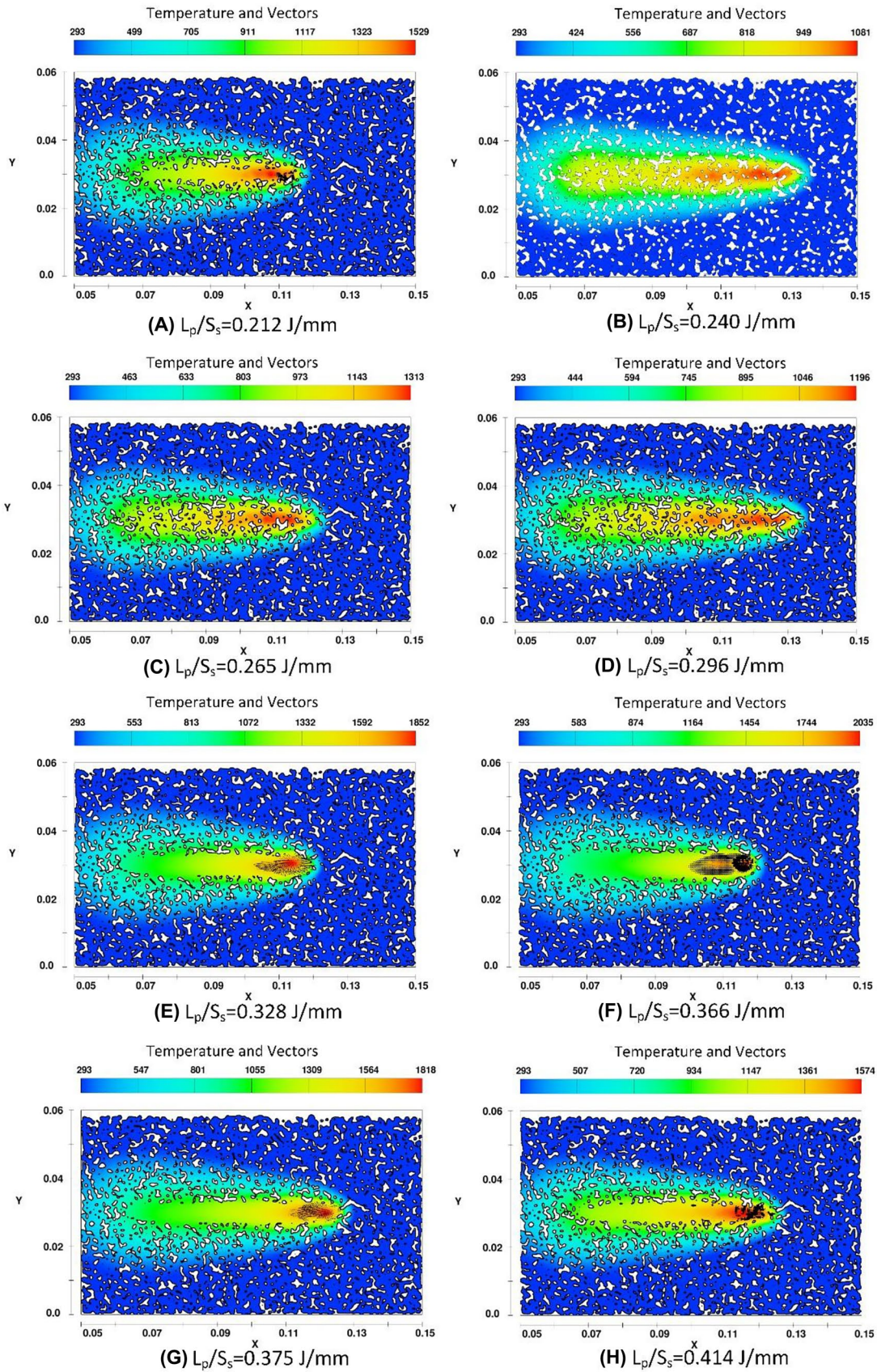


Fig. 2 Simulated meltpool for laser power to scan speed (J/mm): **A** 0.212, **B** 0.240, **C** 0.265, **D** 0.296, **E** 0.328, **F** 0.366, **G** 0.375, **H** 0.414

Table 1 Process parameters and predicted meltpool depth and temperature

Test case	Laser power (W)	Scan speed (mm/s)	Laser power/scan speed (J/mm)	Energy density with absorptivity ratio (J/mm ²)	Energy density without absorptivity ratio (J/mm ³)	Meltpool temperature K	Simulated meltpool depth (μm)
1	225	1060	0.212	63.68	141.51	1102	67
2	255	1060	0.240	72.17	160.38	1205	74
3	255	960	0.265	79.69	177.08	1341	76
4	225	760	0.296	88.82	197.37	1516	85
5	315	960	0.328	98.44	218.75	1618	87
6	315	860	0.366	109.88	244.19	1847	93
7	285	760	0.375	112.50	250.00	1873	94
8	315	760	0.414	124.34	276.32	2048	98

selected. Since the powder particles do not have any movement in the “Y” direction, the “wall” boundary condition was selected for both “ Y_{\min} and Y_{\max} ”. In the “X” direction, the boundary condition was selected “wall” and “outflow” for “ X_{\min} and X_{\max} ” respectively to allow particles to move along with the laser movement. The direction of gravity is specified in the “-Z” axis and the heat exchange between the surfaces of the geometry and shielding gas is defined.

3 Results

3.1 Meltpool depth and temperature profile

The model is developed based on the thermophysical properties of the material. These features are a function of the induced temperature on the meltpool surface. This means that the meltpool temperature for each test case has to be calculated to investigate the related thermophysical properties. The computational software allows for calculating the temperature profile for each test case, as shown in Fig. 2, so the results of the obtained temperature are reported based on the cross-section of the simulated tracks. Eight test cases with different process parameters have been selected in such a way that produces low to high meltpool depth as shown in Table 1. The ratio of laser power to scan speed is changed from 0.212 to 0.414 and the simulated temperature of the meltpool was obtained from 1102.75 to 2048 K. The first three conditions produce a lower temperature than the melting point. The process parameters for test case 4 are designed to target the melting point (1650 K). Test cases 5–8 are aimed for temperatures higher than the melting point. The post-processed simulation results of the melting track for each test case were performed

using FlowSight (i.e., a module developed by Flow3D) and depicted in Fig. 2. The meltpool depth was measured by a lateral cross-section, using the upper surface of the powder bed to the maximum depth of the melt region as reference points. Results reveal that the meltpool depth increases by the ratio of laser power to scan speed from 67.75 to 98.73 μm.

3.2 Developing a model to calculate the meltpool depth

It has been reported [36, 37] that the material properties can affect meltpool features. Therefore, to have a comprehensive model with higher accuracy, a material-based model including thermophysical properties is intended [38]. Process parameters like laser power, scan speed and beam diameter [32, 33, 39] drive meltpool features; thus, the model in this study is developed based on both thermophysical properties and process parameters. According to Table 1, eight simulations have been carried out on a 100-μm powder bed using different laser power to scan speed ratios. The thermophysical properties were calculated from the obtained temperature for each test case as shown in Table 2.

The results of the performed test cases were used to develop a regression model to calculate meltpool depth (MPD) based on process parameters and thermophysical properties of the material. Various regression models were considered, with the best fit obtained using a polynomial regression model (Eq. 5). Where ξ is an experimental coefficient, L_p is the laser power, K is the thermal conductivity, C_p is the specific heat, S_s is the scan speed, and D^e is the density (Table 3). Since most of the LB-PBF have been done in the conduction mode, the regression model has been carried out on this mode.

Table 2 Thermophysical properties of the test cases in the related temperature [40]

Test Case	Density (g/mm ³)	Thermal conductivity (W/mm k)	Specific heat (J/g/k)	Simulation meltpool temperature K
1	7873 × 10 ⁻⁶	24	0.612	1102
2	7833 × 10 ⁻⁶	26	0.636	1205
3	7780 × 10 ⁻⁶	28	0.655	1341
4	7711 × 10 ⁻⁶	31	0.629	1516
5	7391 × 10 ⁻⁶	29	0.720	1618
6	7281 × 10 ⁻⁶	29	0.720	1739
7	7000 × 10 ⁻⁶	29	0.720	2048
8	7210 × 10 ⁻⁶	29	0.720	1818

$$MPD = \frac{\xi \times AR \times L_p^a \times K^b}{C_p^d \times S_s^f \times D^e} \tag{5}$$

To make Eq. (5) gravimetric and to calculate the melt-pool depth in “mm”, the units of ξ were defined as g²/W. Validating the regression model requires the calculation of the *R*-squared and *P*-value. *R*-squared shows the fitness of the regression model. This statistical parameter identifies the percentage of the variance in the dependent/output variable that the independent/input variables explain collectively. *R*-squared measures the strength of the proposed model and the dependent variable. For the presented regression model in Eq. (4), the value of 95.5% was obtained for *R*-squared, which indicates a good fit and accuracy. Another statistical parameter that needs to be checked is the *P*-value that aims at determining the significance of the results to discard the null hypothesis. The null hypothesis states that there is no relationship between the two investigated variables (input and output). The level of significance is expressed by *P*-value, which is between 0 and 1. The smaller the *P*-value (typically ≤ 0.05), the stronger the evidence to reject the null hypothesis, and therefore, the results are statistically significant. In the proposed regression model, the *P*-value obtained was 0.013, which indicates that the null hypothesis can be rejected, and the regression is reliable.

Table 3 Coefficient of the regression model

Coefficient	Numerical values for conduction mode	Numerical values for keyhole mode
ξ	0.0025	0.995
a	0.594	1.060
b	0.292	0.045
d	1.041	0.030
e	1.090	0.026
f	0.411	0.810
AR	30	See Table 5

4 Verification

In this experiment, verification has two steps including validation of simulation and analytical model. First, the accuracy of the simulation is examined by comparing four different simulations with the experimental results (with similar process parameters) from the reported results by Scime [41]. The experimental tests were performed on an EOS M280 LB-PBF machine with 400 W laser power and 100 μm laser diameter at the Arconic Technical Center in New Kensington, Pennsylvania. In the next step, the developed analytical model is examined by feeding the process parameters for four validation tests, and the results are compared with the experimental work. The powder particle size was on average of 25 μm with a packing density of 70%.

4.1 Verification of simulated meltpools

To verify the simulation, four different single tracks have been computationally simulated and the cross-section in Y-direction shows the morphology of the meltpools. The cross-sections presented in Fig. 3 were made from the centre of the Y-axis to show the maximum depth of the meltpool along the X-axis. Figure 3 reveals that the simulation measures the meltpool depth more accurately compared to the experimental tests. This demonstrates a reasonable level of accuracy and reliability on the simulated tracks for further tests and investigations. The layer thickness of both simulation and experimental tests was selected at 70 μm.

4.2 Verification of the developed model

To verify the developed model, four test cases with different process parameters are simulated and presented in Table 4. Here, a ratio of the power to speed of 0.10 to 0.20 was selected to generate a meltpool with different depths.

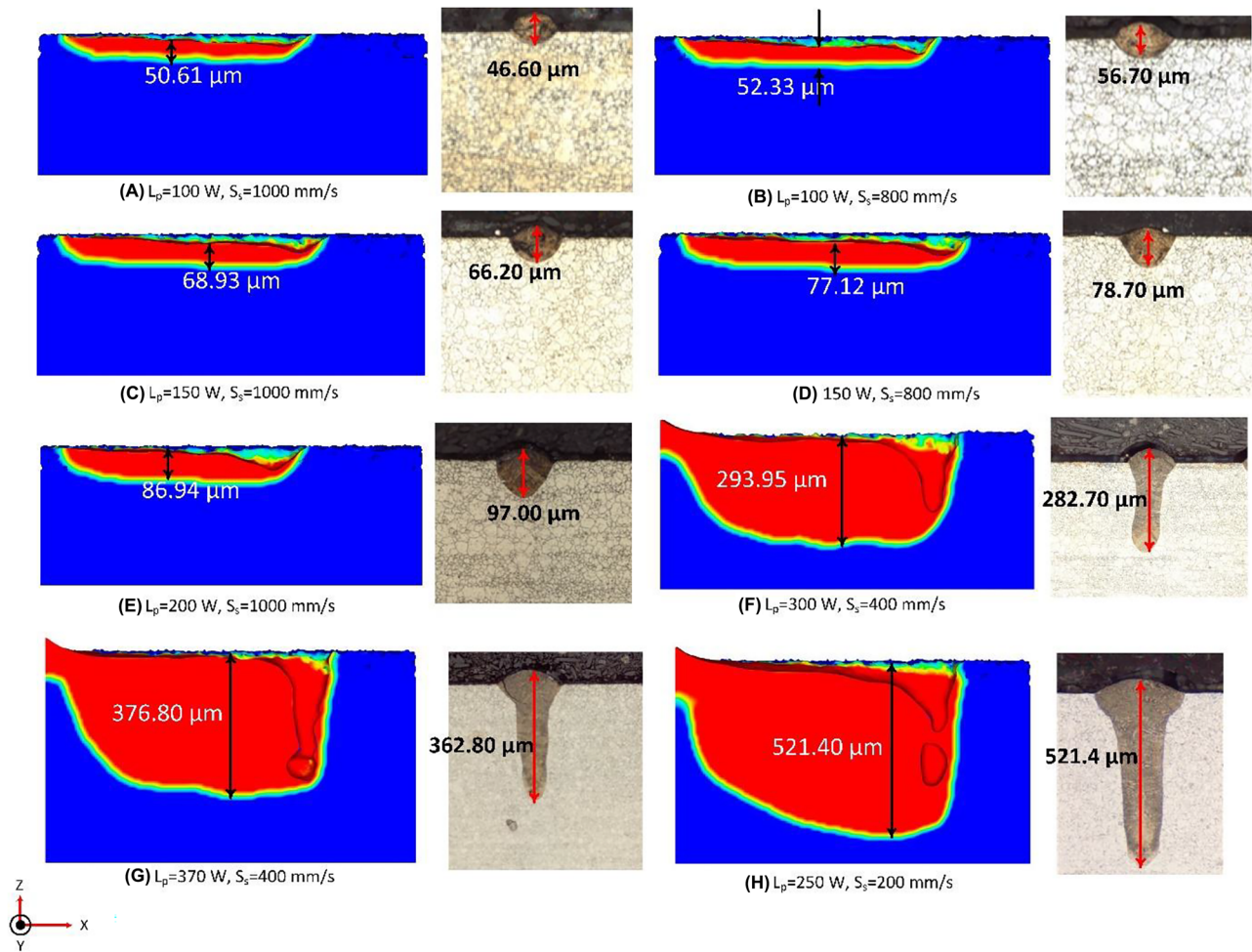


Fig. 3 Y-cross-section for simulated and experimental melt-tracks with different process parameters: **A** $L_p=100$ W, $S_s=1000$ mm/s, **B** $L_p=100$ W, $S_s=800$ mm/s, **C** $L_p=150$ W, $S_s=1000$ mm/s,

D $L_p=150$ W, $S_s=800$ mm/s, **E** $L_p=200$ W, $S_s=1000$ mm/s, **F** $L_p=300$ W, $S_s=400$ mm/s, **G** $L_p=370$ W, $S_s=400$ mm/s, **H** $L_p=250$ W and $S_s=400$ mm/s

In the next step, the melt-pool temperature was calculated, and the related thermophysical properties were extracted for the temperature of each test case. Then, the melt-pool depth was calculated by feeding the process

parameters and obtaining thermophysical properties to Eq. (5) (Table 5).

Figure 4 compares the results of the developed model and simulations versus experimental tests. It can be

Table 4 Process parameters, melt-pool temperature and depth for verification tests

Test case	Laser power (W)	Scan speed (mm/s)	Power/speed (J/mm)	Melt-pool temperature (K)	Simulated melt-pool depth (μm)	Melt-pool mode
9	100	1000	0.1000	1336	50.61	Conduction mode
10	100	800	0.1250	1577	52.33	Conduction mode
11	150	1000	0.1500	1818	68.93	Conduction mode
12	150	800	0.1875	2180	77.12	Conduction mode
13	200	1000	0.2000	2301	86.94	Conduction mode
14	300	400	0.7500	2778	293.95	Keyhole mode
15	370	400	0.9250	5944	376.80	Keyhole mode
16	250	200	1.2500	6549	521.40	Keyhole mode

Table 5 Thermophysical properties of the material in the elevated temperature [40]

Test case	Specific heat (J.g/k)	Density (g/mm ³)	Thermal conductivity (W/mm K)	Absorption ratio (%)
9	0.65	0.00827	28.56	30
10	0.72	0.00739	29.30	30
11	0.72	0.00718	29.30	30
12	0.72	0.00716	29.30	30
13	0.72	0.00716	29.30	30
14	0.72	0.00716	29.30	66.5
15	0.72	0.00716	29.30	68.89
16	0.72	0.00716	29.30	80

observed that the model predicts the meltpool with good accuracy. The maximum error was obtained for the samples with higher laser power to scan speed ratio. The largest error between the predictions and experimental results was calculated at 13.37% while the biggest error between simulations and experimental tests were found to be 11.57%.

5 Discussion

5.1 Transformation of laser energy into heat

The transformation of laser energy in metals has two steps. First, the photons of the laser are absorbed by the electrons of the atoms which increases the internal energy. Then, the high-energy electrons transfer their energy to the atoms in the lattice. When the temperature of the process increases to a sintering state that is 1100 K for Inconel 718 (Test Cases 1 and 2), the energy transfer occurs through surface vibration. The surface vibrations induce less energy to the neighbouring atoms (compared to volumetric vibration), and a shallow meltpool is shaped as shown in Fig. 5. Since the energy density

and temperature are on the surface of the powder bed, the melting is not deep enough. In this condition, the meltpool is shaped at the surface which forms the conduction mode [7, 42].

When the energy density increases to the melting point, the energy transfer occurs through intermolecular vibration. By changing the process parameters to high energy density, chemical bonds are broken directly by stripping the atoms of their electrons by photons. In this situation, the high value of energy density deeply penetrates to the powder bed and previous solidified layers that lead to a shift from conduction mode to keyhole mode, as shown in Fig. 5B.

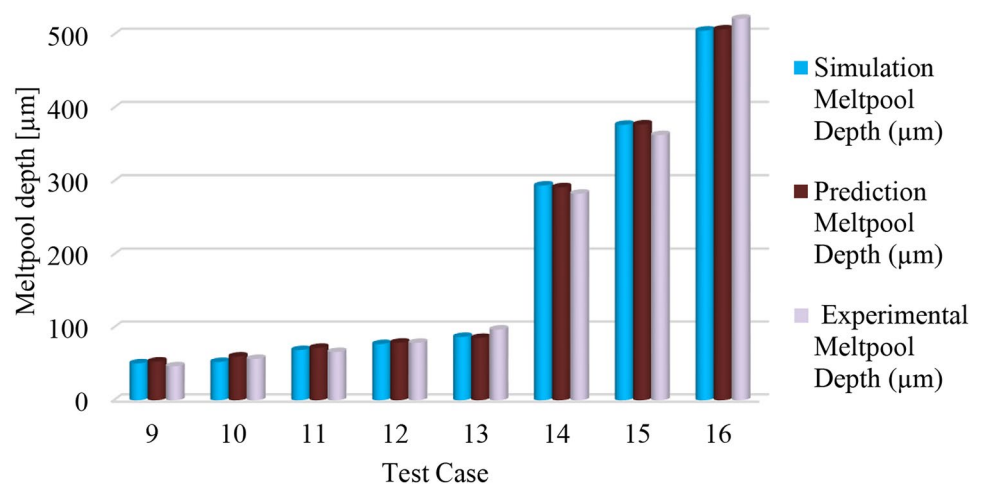
5.2 Driving factors of meltpool depth

5.2.1 Optical penetration depth

The absorption of laser radiation in metals is described by the Beer-Lambert law which states that layers with the same thickness absorb an equal fraction of light (Eq. 6):

$$\frac{dI}{dz} = -\alpha \cdot I \tag{6}$$

Fig. 4 The results of the simulation and analytical model



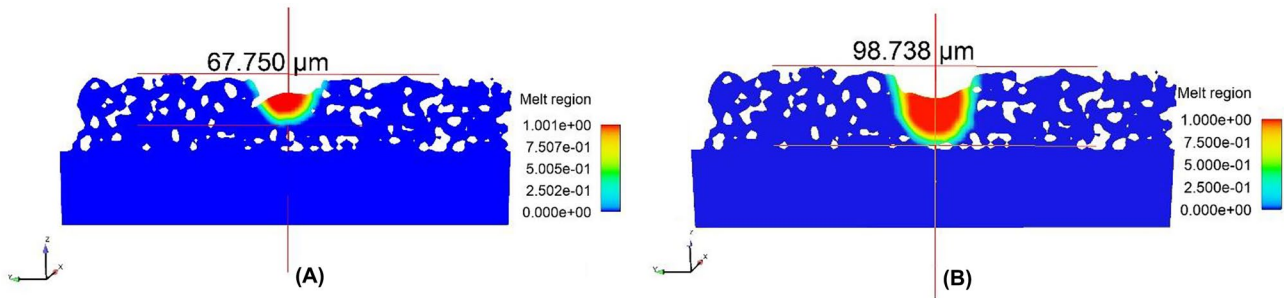


Fig. 5 Energy transfer through the surface and shallow meltpool: **A** test case 1 ($L_p/S_s=0.212$ J/mm) and **B** deep meltpool test case 8 ($L_p/S_s=0.414$ J/mm)

where I is the laser intensity and α is the linear absorption coefficient that is related to the material properties. Beer-Lambert law is obtained from Eq. (7):

$$I(z) = I_0 \cdot e^{-\alpha z} \tag{7}$$

where I_0 is the intensity at the reference point ($z=0$). Based on Beer-Lambert’s law, the intensity versus optical penetration depth was measured and plotted for all test cases. Figure 6 shows that the intensity of the light reduces exponentially with the depth of penetration.

At the powder bed surface ($z=0$), beam intensity is maximum, by increasing z according to Eq. (7), and due to the absorption coefficient of powder, the intensity reduces. For ($z=1$), the intensity has been reduced by $1/e$, or 37% of intimal input energy penetrates the material. When moving further into the bulk of the material $z=2$,

the intensity reduces by the factor of $1/e^2$, or 13% of the initial energy is absorbed in the bulk.

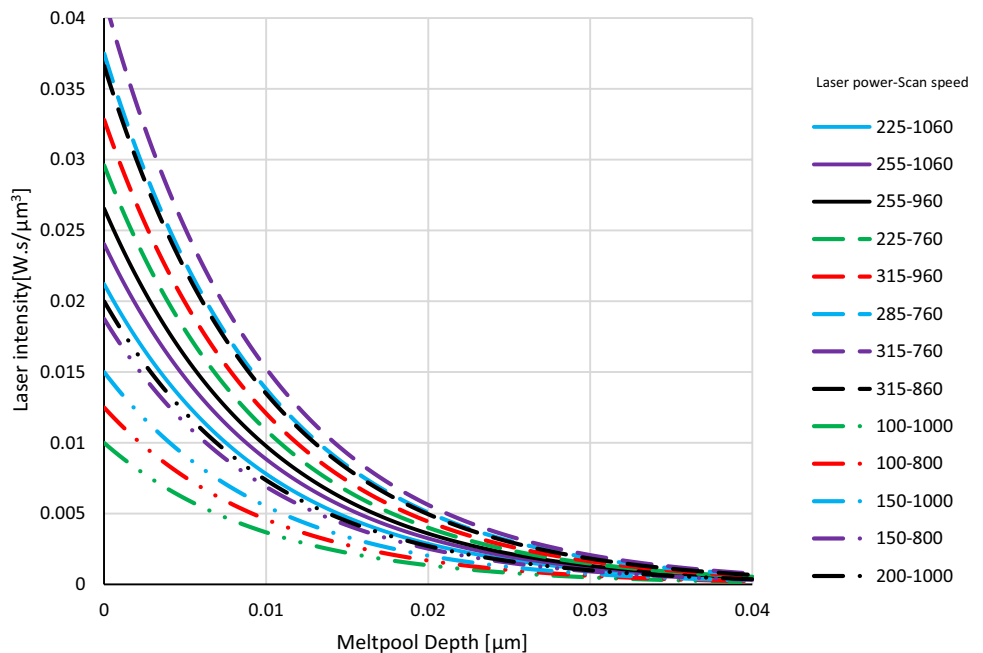
It should be considered that the energy distribution of the beam is defined as Gaussian, and the above-mentioned information is related to the centre of the beam.

Based on Beer-Lambert’s law, the optical penetration depth at the surface and in the bulk is shown through Eq. (8), where α , δ_0 and δ_s are the reflection angle, optical penetration depth at the surface and in the bulk respectively:

$$\delta_0 = \frac{1}{\alpha} \delta_s = \frac{2}{\alpha} \tag{8}$$

Therefore, it shows that the optical penetration depth reduces when penetrating the bulk of the material. This is

Fig. 6 Laser intensity versus meltpool depth for test cases 1–13



the driving factor for the shaping cone shape meltpool in the keyhole mode as can be seen in Figs. 7A and 12.

5.2.2 Angle of incidence

The angle of incidence θ_i of the laser beam and powder bed affects the heat penetration and meltpool depth [33]. For a non-perpendicular incidence angle, the absorptivity is a function of this angle. When processing metals with laser wavelength higher than 500 nm, the absorption A_p [%] for parallel or A_s [%] for perpendicular polarised light is obtained through Eq. (9) [43]:

$$A_p = \frac{4ncos\theta_i}{(n^2+k^2)cos^2\theta_i+2ncos\theta_i+1}, \hat{n} = n + ik$$

$$A_s = \frac{4ncos\theta_i}{n^2+k^2+cos^2\theta_i+2ncos\theta_i+1}, k = \alpha \frac{\lambda}{4\pi}$$
(9)

where “ k ” is the extinction coefficient, “ \hat{n} ” is the refractive index of the material, “ λ ” is the wavelength, and “ i ” is a standard imaginary unit. The value of n and k is obtained from Palik’s Handbook [44].

In this experiment, the incidence angle $\theta_i = 0$ and circularly polarised light were used; thus, the absorption coefficient A_c is obtained from Eq. (10):

$$A_c = \frac{1}{2}(A_p + A_s)$$
(10)

The A_s , for perpendicularly polarised light, reduces by increasing the incidence angle, while A_p first increases to 80% by increasing the incidence angle and radically reduces to zero. The maximum absorptivity is obtained at the incidence angle of 80° . In this experiment, increasing the induced energy density on the surface of the powder bed causes a shift from conduction mode to keyhole mode. As shown in Fig. 7, on the walls of the keyhole, the laser beam penetrates at a larger angle compared to

conduction mode in which $\theta_1 > \theta_2$. This causes parallel polarised light to be strongly absorbed. In this situation, and according to Eq. (8), higher absorptivity is obtained for the keyhole mode that results in inducing higher energy density at the laser interaction point, and as a result, meltpool depth increases. The higher incidence angle for keyhole mode is one of the reasons that a bigger error was found between the proposed analytical model and simulated results in Fig. 4 [43].

5.2.3 The ratio of laser power to scan speed

The ratio of laser power to scan speed is the governing factor for meltpool temperature, and subsequently, the penetration depth. Figure 8A, B show that by increasing the ratio of power to speed from 0.212 to 0.414, a higher energy density raises the temperature of the meltpool from test case 1 to 8. It can be seen in Fig. 8C that the meltpool depth is almost linearly related to the temperature of the meltpool. In the higher range of energy density and temperature, the energy is transferred through intermolecular three-dimensional vibrations in “X”, “Y” and “Z” directions leading to the breaking of chemical bonds of the atomic structures and forming a deeper meltpool.

5.2.4 Surface properties

The surface quality of the material is a significant factor that drives the amount of reflected laser beam and therefore can change the heat penetration and meltpool depth. Previous studies [45–47] showed that the laser power and scan speed dominate the surface quality of LB-PBF components. Increasing laser power leads to increasing

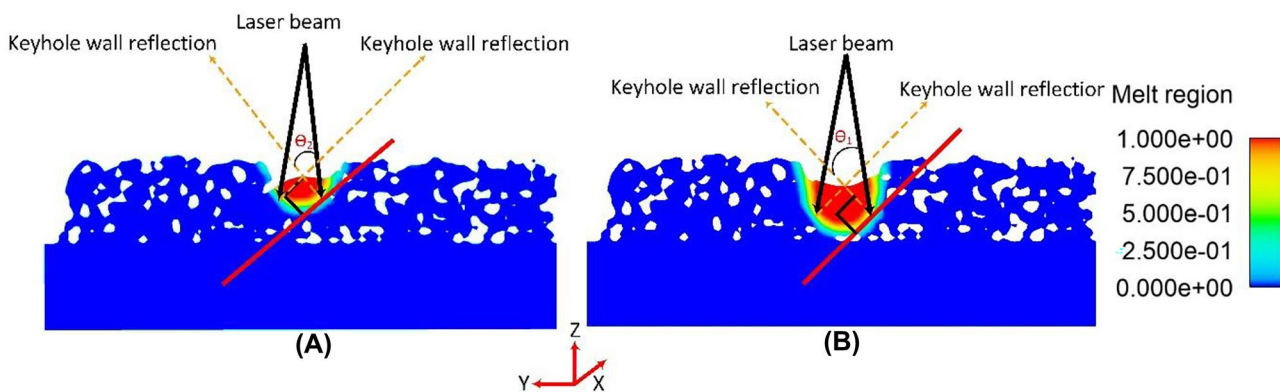


Fig. 7 Keyhole wall reflection **A** cross-section in “X” direction test case 1 ($L_p/S_s=0.212$ J/mm), **B** cross-section in the “X” direction test case 8 ($L_p/S_s=0.414$ J/mm)

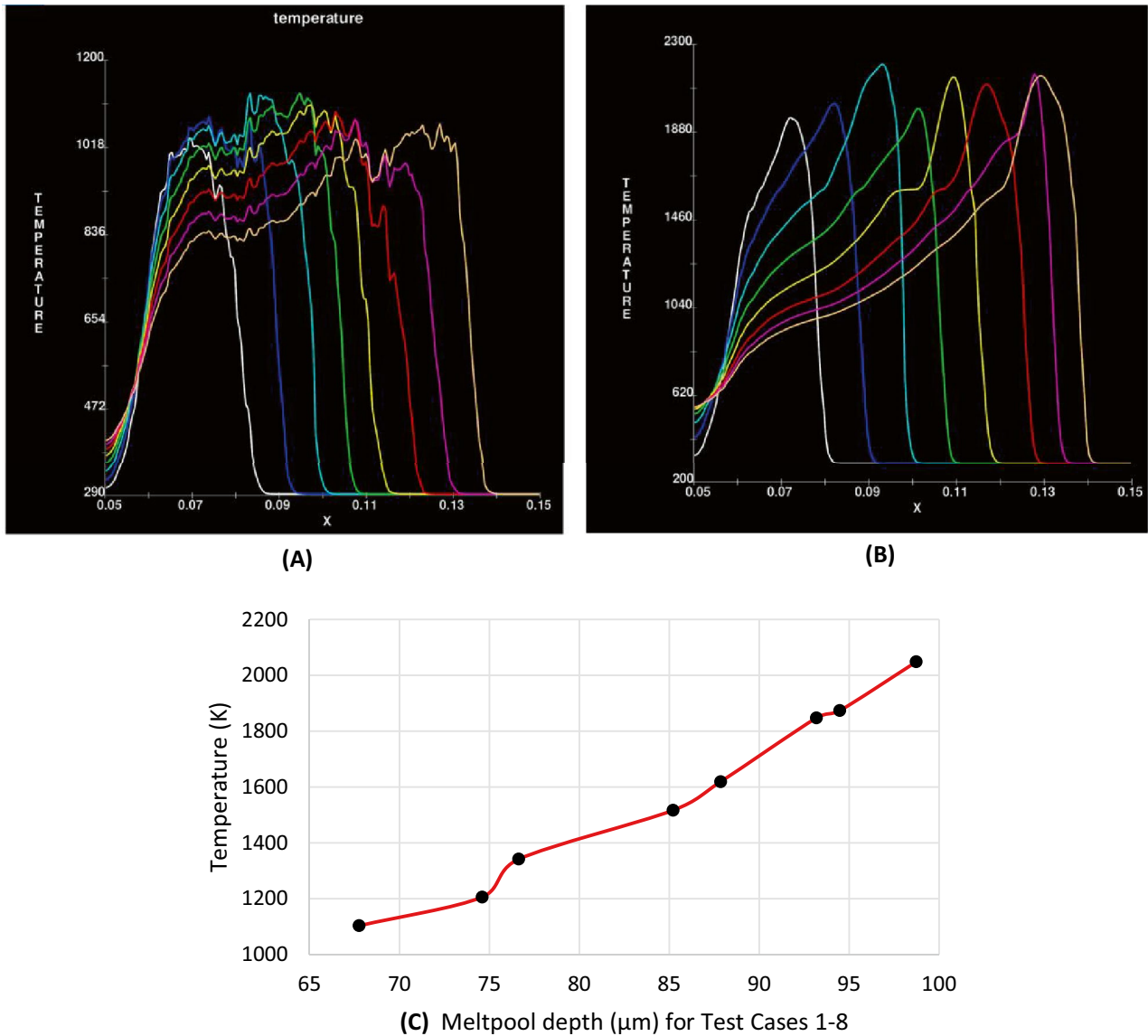


Fig. 8 Meltpool temperature (K) versus length of track (mm) for **A** test case 1 $L_p/S_s = 0.212$ J/mm, **B** test case 8 $L_p/S_s = 0.414$ J/mm, **C** the variation of temperature and meltpool depth

average surface “ S_a ”. Surface roughness is driven by meltpool size and energy density. In the case of a single track, this is highly related to the ratio of laser power to scan speed. For higher energy density, partial melting occurs in a wider area of the powder bed which can cause a formation of peaks and troughs, and therefore a reduction of the surface quality [48]. The width of the track is related to the laser power, scan speed and the interaction of these two parameters. For lower scan speeds and higher laser powers, the meltpool temperature increases, and therefore, wider meltpool areas are

observed (Fig. 9). In this situation, higher Marangoni convection and flow produce a larger mush area and heat-affected zone (HAZ) as can be seen in Fig. 10 [21, 49, 50].

Because the gradient of speed for the melting flow in the mush area is near zero, a higher temperature is accumulated in these regions, which increases the chance of thermal stress by decreasing the surface tension. This provides the ability to form the bow-wave shapes more easily on the surface of the meltpool. Thus, higher energy densities result in rougher surfaces, which is in

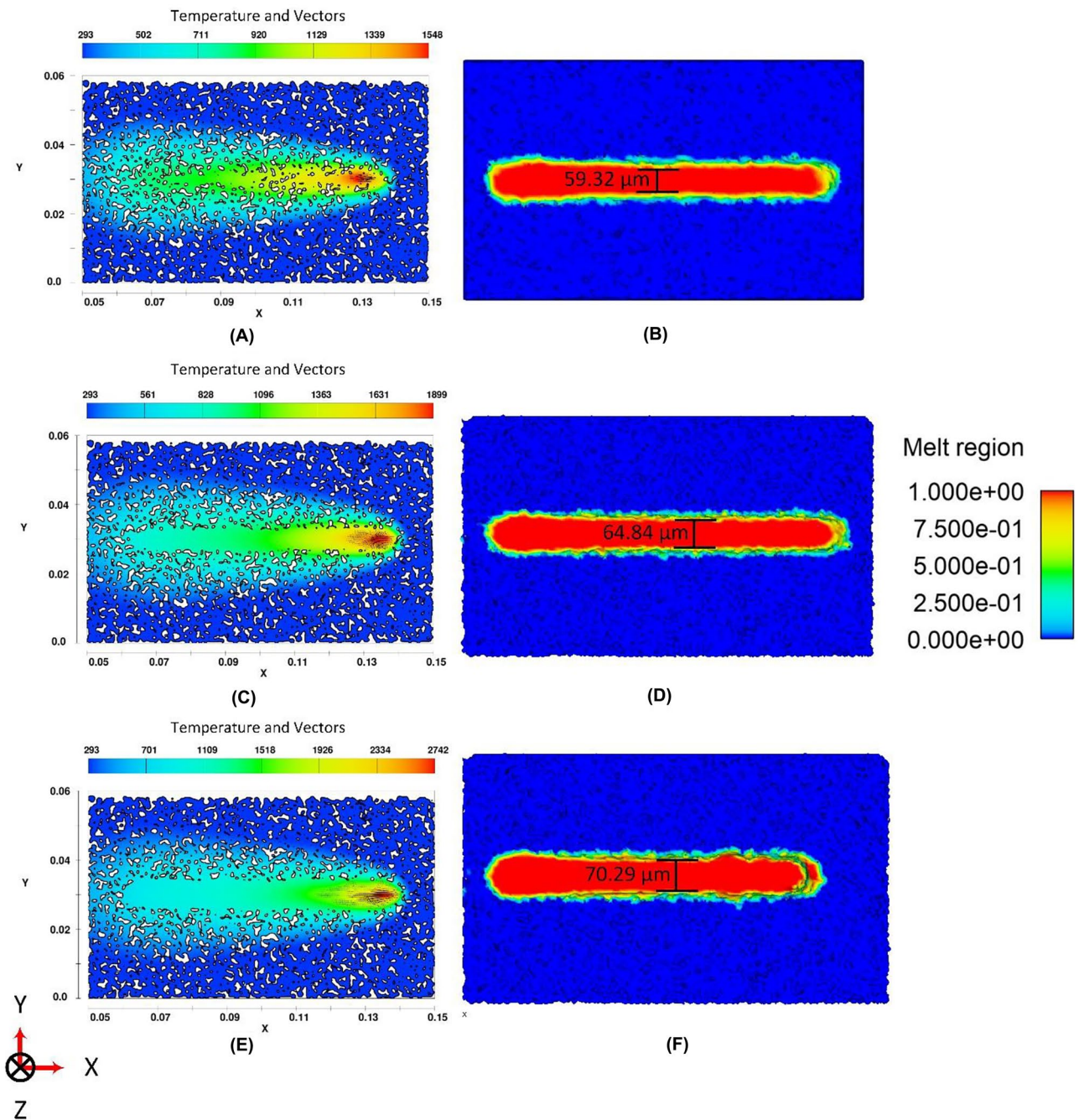


Fig. 9 The width of the melt pool for **A, B** test case 9 $L_p/S_s=0.100$ J/mm, **C, D** test case 4 $L_p/S_s=0.296$ J/mm and **E, F** test case 8 $L_p/S_s=0.414$ J/mm

agreement with similar observations in the literature [51–53].

The chances of creating smooth surfaces in samples with low energy density are higher than in samples with high energy density [46]. Smoother surfaces increase the

reflectivity, which reduces laser beam absorption. In contrast, test cases with higher laser power to scan speed ratio absorb more energy, which also can be attributed to an increase in the incidence angle. Hence, more energy is absorbed, and deeper melt pools are observed, as presented in Tables 1, 4 and Fig. 8.

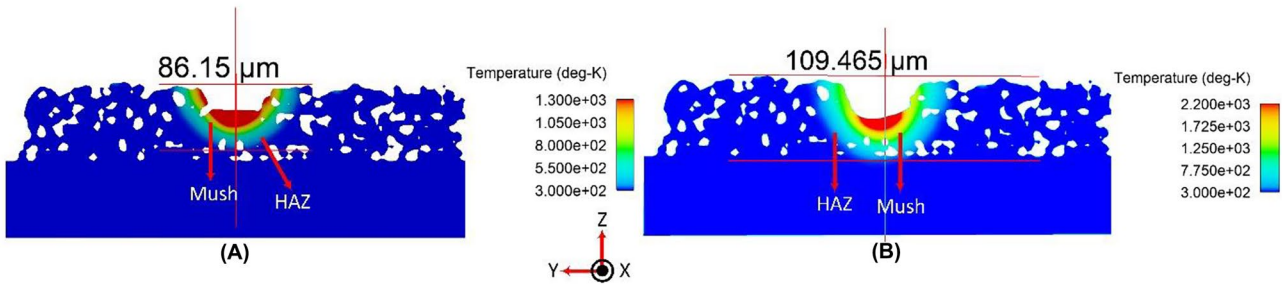


Fig. 10 Heat-affected zone for **A** test case 1 $L_p/S_s=0.212$ J/mm, **B** test case 8 $L_p/S_s=0.414$ J/mm

To analyse the effect of powder on the process, three identical test cases with verification tests have been carried out on bare (solid) substrate. The depth of the melt-pool for the simulation on the bare substrate was found to be slightly higher than the simulation on the powder bed. This may be related to the lower thermal conductivity of the powder bed compared to a solid base plate and/or the enhanced laser absorptivity of powders compared to solid materials. Due to the low thermal conductivity of metallic powder compared to a solid substrate, a fraction of thermal energy that is only conducted downward to the substrate is accumulated and kept in the powder bed. The amount of transferred heat in the X–Y plane for the no-powder condition is slightly higher than the simulation on the powder bed, so the heat transfer in the Z-direction is lower for the no-powder case [54]. Therefore, the depth of melt-pool is slightly lower for powder bed conditions as shown in Fig. 11.

5.2.5 Plasma formation

At high laser intensities (10^{10} – 10^{12} W.m²), vaporisation can occur above the powder bed. Vapour consisting of charged particles such as atoms, ions or electrons conform to the plasma. However, the vapour is referred to as a plume if no charged particles are observed. Both plasma and plume absorb the part of the laser radiation which then transfers to the powder bed or underlying material. Therefore, the total absorption increases compared to test cases with no plume and plasma due to low energy density and temperature. When the laser beam intensity is extremely high (from 10^2 to 10^4 Pa), the plasma and plume density is also high, meaning that almost all the laser light is absorbed by the plasma and plume. Thus, no energy is transferred to the powder bed, and the process is disturbed, and vaporisation and the plasma are no longer fed by the laser stream. This phenomenon extinguishes the plasma and then laser light can reach the powder bed again, and a new plume or plasma can be formed [55, 56]. Repetition of this process generates the pulsed plasma and recoil pressure, which induces more pressure on the laser interaction area and increases the melt-pool depth. The produced plasma from fibre lasers is transparent, so the fraction of the light reaches the surface even with a high density of plume or plasma. If the process parameters are set to induce extremely high energy density, then the mentioned oscillation is undesirable [57]. In the case of vaporisation or plasma formation due to photochemical processes, the material is removed by the (recoil) pressure associated with the vapour or plasma. This leads to an increase in the melt-pool depth in test cases with extremely high energy density and melt-pool temperature as in test case 14 (Table 6). Figure 12 shows the evaporation pressure range for test case 1, 8 and 14 with ratios of laser power to scan speed 0.212, 0.414 and 1.315 J/mm respectively. As can be seen in Fig. 12, the evaporation pressure for test case 14 is 100 and 20 times more than test cases 8 and 1, respectively. Therefore, the depth of the melt-pool is extremely

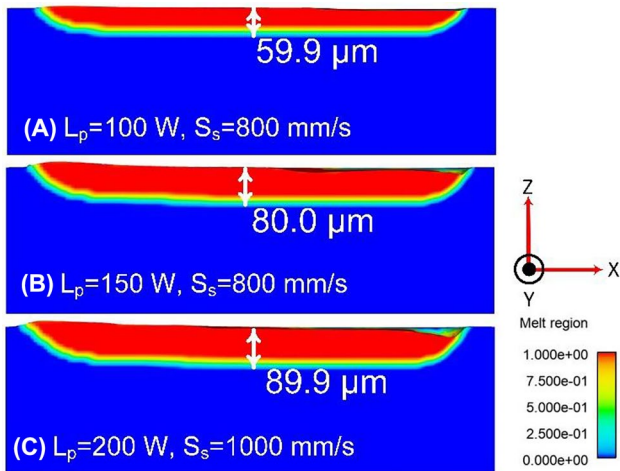
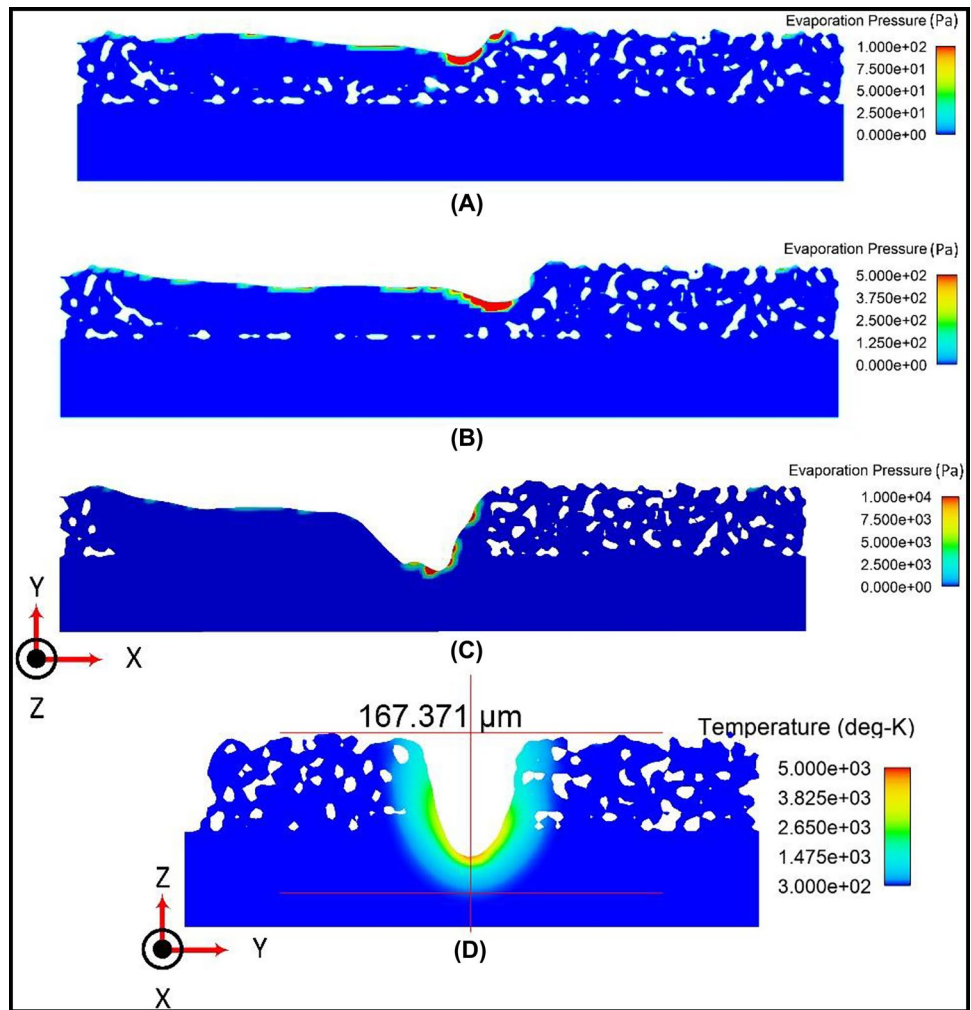


Fig. 11 Simulation on the solid bed showing slightly higher melt-pool depth due to lower thermal conduction in Z-direction

Fig. 12 Evaporation pressure for test cases: **A** Test case 1 $L_p/S_s=0.212$ J/mm, **B** Test case 8 $L_p/S_s=0.414$ J/mm and **C** Test case 14 $L_p/S_s=1.315$ J/mm. **D** Ejection effect due to high energy density for test case 14



higher for this test case compared to the other cases. The high evaporation pressure (Fig. 12D) penetrated and melted a build plate and made a deep HAZ. In addition, due to high recoil pressure for this extreme condition, ejection removed part of the meltpool (Table 6).

However, under normal LB-PBF process conditions, the high plume or plasma density hardly happens, and thus, a fraction of the laser light always reaches the surface of the powder bed.

5.2.6 Statistical analyses of the results

Statistical analyses of the results have been conducted and are discussed to provide more evidence for the presented

Table 6 Conditions of the test case 14

Test case	Laser power (V)	Scan speed (mm/s)	Power/speed (J/mm)	Meltpool temperature (K)
14	1000	760	1.315	6150

results. The results have been obtained based on the depth of the meltpool in the X–Z cross-section. As can be seen in Fig. 13a, all the measurements are located in the vicinity of the probability line. The *P*-value higher than 0.05 indicates the null hypothesis of poor data distribution, so they can be considered as normally distributed data. Figure 13b–d show that by increasing laser power to scan speed ratio, the meltpool depth increases. This is in agreement with Fig. 8C and the presented materials in the discussion and Sect. 5.2.3. Furthermore, according to Eq. (2), increasing laser power and reducing scan speed induces more energy on the surface and forms a deeper meltpool as can be seen in Fig. 13e, f. The 3D and 2D graphs for the variations of the L_p/S_s to the depth of the meltpool show an almost linear increasing trend for the lowest to the highest meltpool depth. This is in agreement with the presented discussion in Sect. 5.2.3 and the found results in Sects. 3.1 and 3.2. The statistical results in this figure prove the developed relation for the energy density reported in Eq. (5).

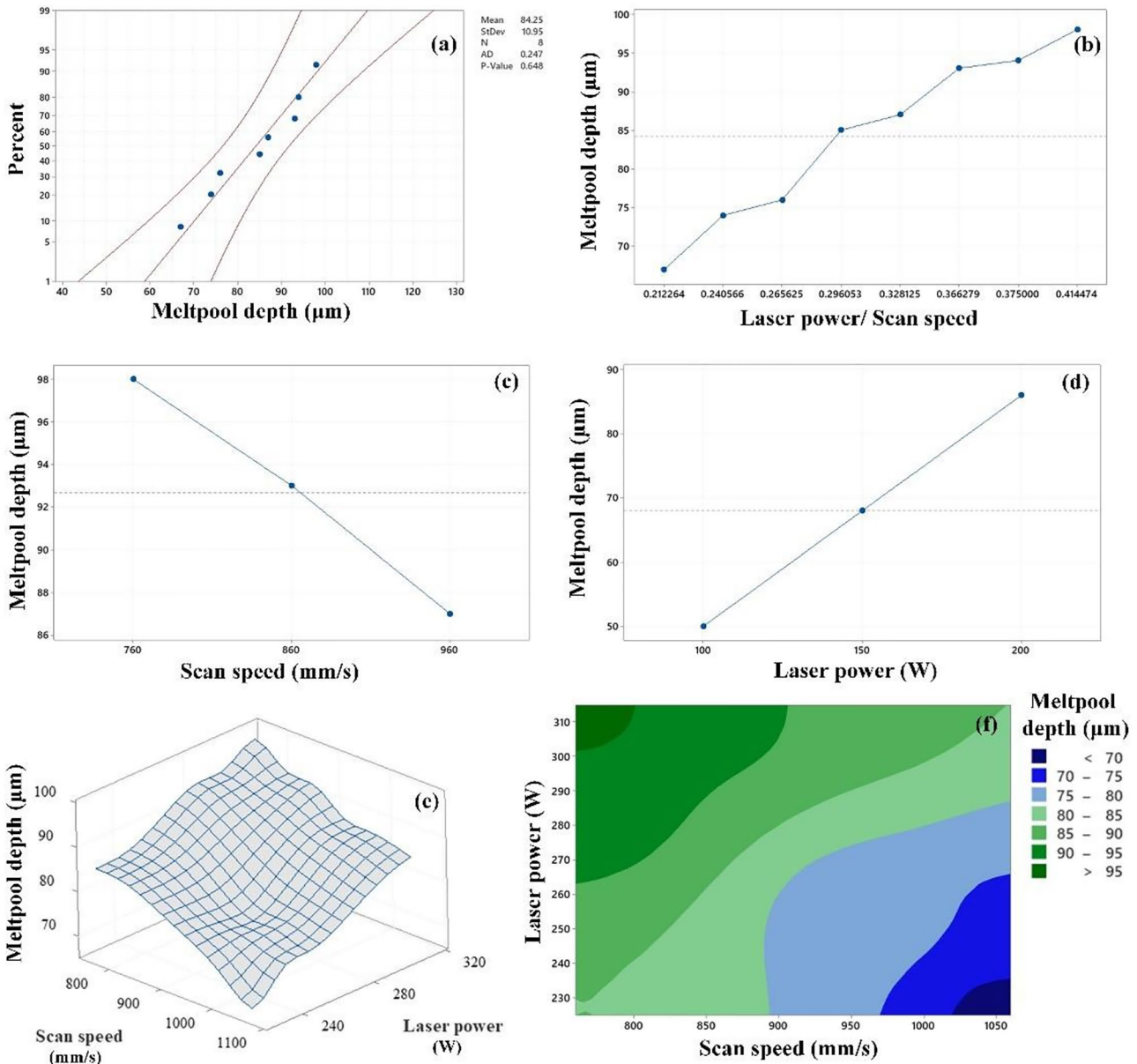


Fig. 13 **a** Probability plot, **b** melt pool depth versus the ratio of L_p/S_s , **c** The effect of increasing laser scan speed in constant laser power on melt pool depth. **d** The effect of increased laser power in constant scan

speed on melt pool depth. **e** 3D surface plot of different scan speed and laser power on melt pool depth. **f** 2D contour plot of different scan speed and laser power on melt pool depth

6 Conclusion

In this research, the fundamental driving factors on the formation of melt pool depth in single track LB-PBF of Inconel 718 were investigated. The effect of optical penetration depth, laser irradiation wavelength, the ratio of laser power to scan speed, angle of incidence, surface properties and plasma formation have been discussed. A set of process parameters was selected to simulate a melt pool with various energy densities using computational software. An analytical model based on the process parameters and thermophysical

properties of the feedstock has been developed to predict the melt pool depth, and the results were experimentally validated.

The results are listed below.

- The presented analytical model is a helpful tool to estimate the process window for desirable depth and bonding before setting process parameters for the printing jobs.
- The depth of melt pool is driven by different factors such as optical penetration depth, irradiation wavelength, angle of incidence, the ratio of laser to speed,

surface roughness and plasma formation. In the lower induced heat and temperature, the high energy atoms transfer their energy through the surface energy. Meanwhile, when the induced heat exceeds a certain value, the energy transfer is carried out by intermolecular vibration which breaks the chemical bonding and increases the depth of the meltpool.

- The optical penetration depth reduces in the bulk of the material, which is the driving factor to form a cone shape meltpool in keyhole mode.
- On the keyhole walls, the laser beam penetrates at a bigger angle in comparison with conduction mode which increases parallel absorption coefficient and subsequently the heat and depth of the meltpool.
- Using lower power to speed produces smoother surfaces that have more reflection and reduces absorptivity and meltpool depth.
- Both plasma and plume absorb a fraction of the laser radiation which is transferred to the powder bed or underlying solidified layers. This increases the total absorption for the test cases with higher energy density and temperature. When the laser beam intensity is extremely high, the density of the vapour and plasma increases (from 10^2 to 10^4 Pa) and absorbs a big fraction of the laser energy and disturbs the energy transmission to the powder bed. In this condition, plasma or vapour is no longer fed by the laser stream and is extinguished, allowing the laser light to reach the powder bed again and form the plume and plasma. Alternation of this process produces pulsed recoil pressure which changes the meltpool morphology and increases the meltpool depth.

Future directions Future work can be dedicated towards analysing the effect of heat transfer through the powder particle and the building substrate versus the generated heat modes including conduction and keyhole. The interaction of the heat modes and conduction heat transfer can provide valuable information on the thermal history of the processed materials and is useful for the prediction of the thermal residual stresses.

Acknowledgements The authors acknowledge Dr. Luke Scime for his supports and help on experimental verifications. All the authors have read and approved the presented materials in the paper and acknowledged the received supports.

Author contribution Dr. Mahyar Khorasani, Dr. Laura Cordova and Dr. Ehsan Farabi contributed to writing and proofreading the manuscript. Mr. AmirHossein Ghasemi and Mrs. Elmira Sharabian helped to draw the figures and write the manuscript. Professor Ian Gibson and Professor Martin Leary contributed to writing. Professor Milan Brandt and Professor Bernard Rolfe contributed to writing and proofreading the manuscript.

Declarations

Ethics approval Not applicable.

Consent to participate Not applicable.

Consent for publication Not applicable.

Competing interests The authors declare no competing interests.

Open Access This article is licensed under a Creative Commons Attribution 4.0 International License, which permits use, sharing, adaptation, distribution and reproduction in any medium or format, as long as you give appropriate credit to the original author(s) and the source, provide a link to the Creative Commons licence, and indicate if changes were made. The images or other third party material in this article are included in the article's Creative Commons licence, unless indicated otherwise in a credit line to the material. If material is not included in the article's Creative Commons licence and your intended use is not permitted by statutory regulation or exceeds the permitted use, you will need to obtain permission directly from the copyright holder. To view a copy of this licence, visit <http://creativecommons.org/licenses/by/4.0/>.

References

1. Gibson I et al (2021) Additive manufacturing technologies. 3rd ed. Springer
2. ASTM International (2015) ISO/ASTM52900–15, Standard terminology for additive manufacturing – general principles – terminology. ASTM International, West Conshohocken, PA
3. Sun S, Brandt M, Easton M (2017) Powder bed fusion processes: An overview. *Laser Addit Manuf* 55–77
4. Milewski JO (2017) Additive manufacturing of metals. Springer International Publishing, Cham
5. Zhao C et al (2017) Real-time monitoring of laser powder bed fusion process using high-speed X-ray imaging and diffraction. *Sci Rep* 7(1):1–11
6. Raghavan N et al (2016) Numerical modeling of heat-transfer and the influence of process parameters on tailoring the grain morphology of IN718 in electron beam additive manufacturing. *Acta Mater* 112:303–314
7. Khairallah SA et al (2016) Laser powder-bed fusion additive manufacturing: physics of complex melt flow and formation mechanisms of pores, spatter, and denudation zones. *Acta Mater* 108:36–45
8. King WE et al (2014) Observation of keyhole-mode laser melting in laser powder-bed fusion additive manufacturing. *J Mater Process Technol* 214(12):2915–2925
9. King W et al (2015) Overview of modelling and simulation of metal powder bed fusion process at Lawrence Livermore National Laboratory. *Mater Sci Technol* 31(8):957–968
10. Criales LE et al (2017) Laser powder bed fusion of nickel alloy 625: experimental investigations of effects of process parameters on melt pool size and shape with spatter analysis. *Int J Mach Tools Manuf* 121:22–36
11. Scime L, Beuth J (2019) Melt pool geometry and morphology variability for the Inconel 718 alloy in a laser powder bed fusion additive manufacturing process. *Addit Manuf* 29:100830
12. Scime L, Beuth J (2019) Using machine learning to identify in-situ melt pool signatures indicative of flaw formation in a

- laser powder bed fusion additive manufacturing process. *Addit Manuf* 25:151–165
13. Hooper PA (2018) Melt pool temperature and cooling rates in laser powder bed fusion. *Addit Manuf* 22:548–559
 14. Zhang Z et al (2019) 3-Dimensional heat transfer modeling for laser powder-bed fusion additive manufacturing with volumetric heat sources based on varied thermal conductivity and absorptivity. *Opt Laser Technol* 109:297–312
 15. Patel S, Vlasea M (2020) Melting modes in laser powder bed fusion. *Materialia* 9:100591
 16. Keshavarzkermani A et al (2019) An investigation into the effect of process parameters on melt pool geometry, cell spacing, and grain refinement during laser powder bed fusion. *Opt Laser Technol* 116:83–91
 17. Aversa A et al (2018) Single scan track analyses on aluminium based powders. *J Mater Process Technol* 255:17–25
 18. Ye J et al (2019) Energy coupling mechanisms and scaling behavior associated with laser powder bed fusion additive manufacturing. *Adv Eng Mater* 21(7):1900185
 19. Reijonen J et al (2020) On the effect of shielding gas flow on porosity and melt pool geometry in laser powder bed fusion additive manufacturing. *Addit Manuf* 32:101030
 20. Demir AG et al (2019) Complementary use of pulsed and continuous wave emission modes to stabilize melt pool geometry in laser powder bed fusion. *Opt Laser Technol* 113:15–26
 21. Karayagiz K et al (2019) Numerical and experimental analysis of heat distribution in the laser powder bed fusion of Ti-6Al-4V. *IJSE Trans* 51(2):136–152
 22. Foroozmehr A et al (2016) Finite element simulation of selective laser melting process considering optical penetration depth of laser in powder bed. *Mater Des* 89:255–263
 23. Wang W, Ning J, Liang SY (2021) Prediction of lack-of-fusion porosity in laser powder-bed fusion considering boundary conditions and sensitivity to laser power absorption. *Int J Adv Manuf Technol* 112(1):61–70
 24. Yan W et al (2018) Meso-scale modeling of multiple-layer fabrication process in selective electron beam melting: inter-layer/track voids formation. *Mater Des* 141:210–219
 25. Gibson I et al (2021) *Additive manufacturing technologies*. 3rd ed. Springer 675
 26. de Oliveira AR et al (2021) Compression and energy absorption of maraging steel primitive scaffolds produced by powder bed fusion. *Int J Adv Manuf Technol* 1–13
 27. Cunningham R et al (2019) Keyhole threshold and morphology in laser melting revealed by ultrahigh-speed x-ray imaging. *Science* 363(6429):849–852
 28. Shrestha S, Chou K (2021) An investigation into melting modes in selective laser melting of Inconel 625 powder: single track geometry and porosity. *Int J Adv Manuf Technol* 1–13
 29. Fabbro R, Chouf K (2000) Keyhole modeling during laser welding. *J Appl Phys* 87(9):4075–4083
 30. Ren Y, Wang Q (2021) Gaussian-process based modeling and optimal control of melt-pool geometry in laser powder bed fusion. *J Intell Manuf* 1–18
 31. Wang H, Zhang Y, Chen K (2016) Modeling of temperature distribution in laser welding of lapped martensitic steel M1500 and softening estimation. *J Manuf Sci Eng* 138(11)
 32. Kamath C et al (2014) Density of additively-manufactured, 316L SS parts using laser powder-bed fusion at powers up to 400 W. *Int J Adv Manuf Technol* 74(1–4):65–78
 33. Gibson I et al (2021) *Powder bed fusion*. *Addit Manuf Technol*. Springer, Cham, pp 125–170
 34. Wolff SJ et al (2019) Experimentally validated predictions of thermal history and microhardness in laser-deposited Inconel 718 on carbon steel. *Addit Manuf* 27:540–551
 35. Khorasani M et al (2021) Numerical and analytical investigation on meltpool temperature of laser-based powder bed fusion of IN718. *Int J Heat Mass Trans* 177:121477
 36. Teng C et al (2016) The effects of material property assumptions on predicted meltpool shape for laser powder bed fusion based additive manufacturing. *Meas Sci Technol* 27(8):085602
 37. Waqar S et al (2021) Numerical investigation of thermal behavior and melt pool morphology in multi-track multi-layer selective laser melting of the 316L steel. *Int J Adv Manuf Technol* 112(3):879–895
 38. Philo A et al (2019) A pragmatic continuum level model for the prediction of the onset of keyholing in laser powder bed fusion. *Int J Adv Manuf Technol* 101(1–4):697–714
 39. Gibson I et al (2021) *Development of additive manufacturing technology*. *Addit Manuf Technol*. Springer, pp 23–51
 40. Mills KC (2002) *Recommended values of thermophysical properties for selected commercial alloys*. Woodhead Publishing
 41. Scime LR (2018) *Methods for the expansion of additive manufacturing process space and the development of in-situ process monitoring methodologies*. Carnegie Mellon University
 42. Gibson I et al (2020) *Additive manufacturing technologies*. 3rd ed. Springer
 43. Romer GW (2016) *Laser material processing*. The University of Twente 1–291
 44. Palik ED (1998) *Handbook of optical constants of solids*. Vol. 3. Academic press
 45. Khorasani AM et al (2020) Modelling of laser powder bed fusion process and analysing the effective parameters on surface characteristics of Ti-6Al-4V. *Int J Mech Sci* 168:105299
 46. Khorasani A et al (2019) The effect of SLM process parameters on density, hardness, tensile strength and surface quality of Ti-6Al-4V. *Addit Manuf* 25:176–186
 47. Clijsters S et al (2014) In situ quality control of the selective laser melting process using a high-speed, real-time melt pool monitoring system. *Int J of Adv Manuf Technol* 75(5–8):1089–1101
 48. Safdar A et al (2012) Effect of process parameters settings and thickness on surface roughness of EBM produced Ti-6Al-4V. *Rapid Prototyp J*
 49. Liang Z et al (2020) Development of computational framework for titanium alloy phase transformation prediction in laser powder-bed fusion additive manufacturing. *Materialia* 14:100934
 50. Gibson I et al (2021) *Directed energy deposition*. *Addit Manuf Technol*. Springer, Cham, pp 285–318
 51. Sing SL, Yeong WY, Wiria FE (2016) Selective laser melting of titanium alloy with 50 wt% tantalum: Microstructure and mechanical properties. *J Alloy Compd* 660:461–470
 52. Martinez R, Todd I, Mumtaz K (2019) In situ alloying of elemental Al-Cu12 feedstock using selective laser melting. *Virtual Phys Prototyp* 14(3):242–252
 53. Teixeira O, Silva FJ, Atzeni E (2021) Residual stresses and heat treatments of Inconel 718 parts manufactured via metal laser beam powder bed fusion: an overview. *Int J Adv Manuf Technol* 1–24
 54. Gong H et al (2014) Melt pool characterization for selective laser melting of Ti-6Al-4V pre-alloyed powder. In 2014 International Solid Freeform Fabrication Symposium. University of Texas at Austin
 55. Schaaf P (2010) *Laser processing of materials: fundamentals, applications and developments* Vol. 139. Springer Science & Business Media
 56. Gibson I et al (2021) *Materials for additive manufacturing*. *Addit Manuf Technol*. Springer, pp 379–428
 57. Bäuerle D (2013) *Laser processing and chemistry*. Springer Science & Business Media

Publisher's note Springer Nature remains neutral with regard to jurisdictional claims in published maps and institutional affiliations.